

Super-exchange mechanism and quantum many body excitations in the archetypal hemocyanin/tyrosinase di-Cu oxo-bridge

Mohamed Ali al-Badri,¹ Edward Linscott,² Antoine Georges,^{3,4,5,6} Daniel J. Cole,⁷ and Cédric Weber¹

¹*King's College London, Theory and Simulation of Condensed Matter (TSCM), Strand, London WC2R 2LS, United Kingdom*

²*Cavendish Laboratory, University of Cambridge, J. J. Thomson Avenue, Cambridge CB3 0HE, United Kingdom*

³*Collège de France, 11 place Marcelin Berthelot, 75005 Paris, France*

⁴*Center for Computational Quantum Physics, Flatiron Institute, 162 Fifth avenue, New York, NY 10010, USA*

⁵*CPHT, Ecole Polytechnique, CNRS, Université Paris-Saclay, 91128 Palaiseau, France*

⁶*DQMP, Université de Genève, 24 quai Ernest Ansermet, CH-1211 Genève, Suisse*

⁷*School of Natural and Environmental Sciences, Newcastle University, Newcastle upon Tyne NE1 7RU, United Kingdom*

We perform first-principles quantum mechanical studies of dioxygen ligand binding to the hemocyanin protein. Electronic correlation effects in the functional site of hemocyanin are investigated using a state-of-the-art approach, treating the localized copper $3d$ electrons with cluster dynamical mean field theory (DMFT) for the first time. This approach has enabled

us to account for dynamical and multi-reference quantum mechanics, capturing valence and spin fluctuations of the 3d electrons. Our approach predicts the stabilization of a quantum entangled di-Cu singlet in the London-Heitler limit, with localized charge and incoherent scattering processes across the oxo-bridge, that prevent long-lived charge excitations. This suggests that the magnetic structure of hemocyanin is largely influenced by the many-body corrections. Our computational model is supported by remarkable agreement with experimental optical absorption data, and provides a revised understanding of the bonding of the peroxide to the di-Cu system.

Copper-based metalloproteins play a major role in biology as electron or dioxygen (O_2) transporters. Hemocyanin (Hc) is one of three oxygen transporting proteins found in nature, alongside the iron-based hemerythrin and hemoglobin, and is common to a number of invertebrates, such as molluscs and arthropods. Deoxy-Hc employs two half-spin copper (I) cations, each coordinated by the imidazole rings of three histidine residues, to reversibly bind O_2 . An accurate understanding of the electronic structure (spin and charge) of the Cu_2O_2 core is essential to clarifying the operation of dioxygen transport as well as the catalytic mechanisms of type 3 copper-based enzymes such as tyrosinase and catechol oxidase, or multicopper oxidases.^{1,2} A theoretical understanding of this mechanism would advance the design of synthetic catalysts that employ dioxygen as a terminal oxidant. There is significant interest in the biomimetic application of naturally occurring metal complexes for the use in metallodrug design, with Cu(II) complexes recently employed in cancer therapeutics as artificial DNA metallonucleases³ and tyrosinase mimics.⁴

However, the formation of oxygenated hemocyanin (oxyHc) via the binding of O_2 to deoxygenated hemocyanin (Hc) remains a challenging problem, and key questions remain unresolved. In particular, the binding of O_2 falls into the category of a spin-forbidden transition. Molecular O_2 is in a spin triplet configuration, and the Cu ions in deoxyHc are known to be in the Cu(I) d^{10} singlet configuration. The combination of triplet O_2 and singlet deoxyHc, to produce the Cu_2O_2 antiferromagnetic singlet in oxyHc, is believed to occur via a simultaneous charge transfer of one electron from each Cu(I) ion to O_2 forming a hybrid Cu(II)-peroxy-Cu(II) configuration. Hence a super-exchange pathway is hypothesized to form across the two Cu atoms.⁵ This mechanism is supported by SQUID measurements that report a large super-exchange coupling⁶ between the two Cu centers, and a diamagnetic ground state.⁷

Despite intensive theoretical studies on the nature of the side-on coordinated Cu_2O_2 core, theoretical analysis has so far proved to be challenging for many electronic structure methods including *ab initio* quantum chemistry, density functional theory (DFT) and mixed quantum/classical (QM/MM) methods due to the complex simultaneous interplay of both the charge and spin, and to the multi-reference character of oxyHc. In particular, DFT and hybrid-DFT do not predict the correct singlet ground state,⁸⁻¹⁰ due to the multi-reference nature of the ground state that is not accessible in DFT-based approaches. To overcome the limitation of DFT techniques, a spin-projection method (also called spin-mixing) has been applied, wherein the different spin-polarized ground states are calculated individually,¹¹ and the entangled singlet is reconstructed by linear combination of the respective Slater determinants (essentially a combination of the spin-broken symmetry state in the up-down, up-up, down-down configurations to extract an effective singlet

state). Although this construction yields insights into the energetics, it does not allow for the study of excitations, and limits the scope of comparison with experimental data, such as the optical absorption,⁹ that is a stringent test of any theory. Furthermore, the spin-contamination present in spin-polarized hybrid DFT remains an issue,^{5,10,12–14} and typically the broken symmetry state becomes asymmetric in the oxyHc Cu₂O₂ core,⁹ which is an artefact of the method used. Finally, experiments have also alluded to the necessity of characterizing the oxyHc ground state as a mixed valence state,¹⁵ which cannot be accessed in the ground state DFT approach.

In this work, we apply for the first time an extension of DFT, dynamical mean-field theory (DMFT¹⁶), that accounts for all the limitations discussed above, and treats non-perturbatively the many-body effects and the super-exchange of the di-Cu bridge. DMFT is a sophisticated method that includes quantum dynamical effects, and takes into account both valence and spin fluctuations, and thermal excitations. Although DMFT is routinely used to describe materials, it was also recently extended to molecular systems,^{17,18} and combined with the linear-scaling DFT software, ONETEP, to extend the applicability of DFT+DMFT to systems of unprecedented size.^{19–23} Here, we systematically study how the Coulomb repulsion term U , which is absent from DFT, corrects the magnetic properties of oxyHc. We report the quantum entangled low energy states and analyze the dominant contributions to the charge and magnetic properties of Cu₂O₂. This enables the identification of the regime of parameters where the singlet is stabilized ($U = 6 - 8$ eV), and the renormalization of the diamagnetism induced by quantum fluctuations. We show that a dominant spin singlet state is maximized at $U = 8$ eV and discuss the validation of the model by optical experiments. The obtained singlet is in the Heitler-London regime (entangled quantum superposition

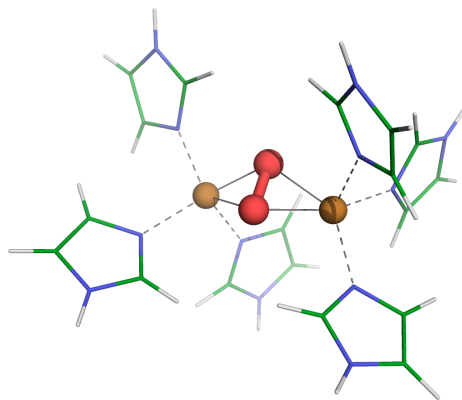


Figure 1: The oxyHc functional complex, showing the Cu_2O_2 correlated subsystem, which is treated using DMFT, and the surrounding imidazole rings representing the protein environment.

of two localized magnetic moments), and is associated with incoherent scattering processes that reduce the lifetime of charge excitations.

Results

In the present work, we perform the first DFT + DMFT simulations on a 58-atom model of the oxyHc functional complex (Fig. 1). Although previous DFT-based approaches have reported that a di-Cu singlet is obtained across the oxo-bridge, these approaches invoke artificial constructions to overcome the single-Slater determinant approach of DFT. Instead, we hereby treat the multi-reference, finite-temperature and explicit on-site Coulomb interaction effects associated with the Cu $3d$ binding site, in single, self-consistent calculations, and systematically investigate how the Hubbard Coulomb potential U alters the electronic structure at the Cu_2O_2 site.

As this problem involves direct exchange across two correlated atoms, we use the non-local

DMFT implementation (cluster DMFT), needed to characterize the superexchange mechanism between the Cu_2 d -orbitals and intermediate p -orbitals, as single site DMFT can only treat the multiplet structure of each Cu atom separately. In its simplest form, DMFT invokes a mean-field approximation across the multiple correlated sites, which is not the case in our approach, as all correlated sites are directly treated in the multi-site Anderson impurity model (AIM). Hence our approach might be denoted as DFT+AIM. Note however that we do carry out a self-consistency cycle over the charge density, as we work at fixed total number of electrons, and this produces a feedback to the solution of the model that is similar in its nature to the mean-field approximation used in DMFT. We consider the the Hubbard U coupling in the range $U = 0$ to 10 eV. The Hubbard U correction is known to be paramount to describe many-body effects responsible for the superexchange process across Cu atoms. Several competing effects stem from the local Hubbard U physics: charge localization, exchange of electrons, charge-transfer excitations, and stabilization of magnetic multiplets. Although typical values for U can be obtained by linear response or constrained RPA,²⁴ these predictions are typically dependent on the choice of local orbitals and basis representation. We instead consider a range of values; by artificially manipulating the magnitude of the local many-body effects, we can investigate their influence on the electronic spectral weight and magnetic properties. A typical value of U for the $3d$ electrons of Cu is 8–8.5 eV.^{25,26}

Charge and spin fluctuations. We first turn to the study of the charge and spin fluctuations induced by the Coulomb repulsion U . We calculated the reduced density matrix of the di-Cu system, and the weight of the obtained eigenvectors, which correspond to the possible excitations of the system (Fig. 2). This provides a detailed picture of the electronic structure of the $3d$ subspace

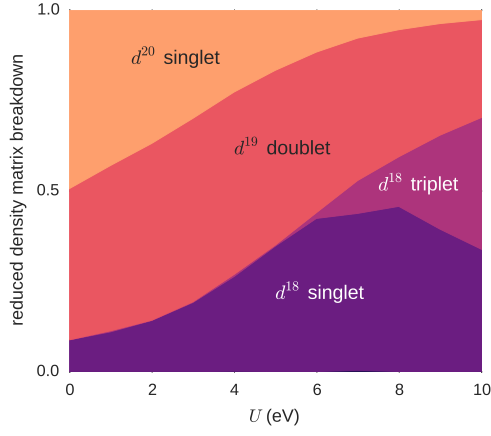


Figure 2: Decomposition of the reduced density matrix of the Cu_2 dimer in the different quantum sectors. The colors corresponds to the respective weights of the different contributions for each value of the Coulomb repulsion U (if a color occupies all the vertical axis, for example, it means that all eigenvectors of the density matrix are in the same quantum sector). Note that the d occupation is the sum of both Cu sites (for example, d^{20} means the two Cu atoms are respectively in the d^{10} configuration).

of the Cu atoms. Within DMFT, the density matrix is obtained by tracing the Anderson impurity model over the bath degrees of freedom, and gives an effective representation of the quantum states of the two Cu atoms. Note that in our approach, the ground-state wave-function is not a pure state with a single allowed value for the spin states (singlet, doublet, triplet, etc.), yet we can describe the fluctuating spin states of the Cu atom by analyzing the spin distribution obtained from the dominant configurations. In the weakly correlated regime ($U < 2$ eV), we obtain a large contribution from the d^{20} and d^{19} configurations, indicating that the average charge transfer from the Cu to O_2 involves less than $1e$ per Cu, thus preventing the formation of a singlet (as the Cu $3d$ orbitals are nearly full).

Diamagnetism. As U increases the total electronic occupation of the Cu dimer decreases (Fig. 2 and Table 1). In the range $U = 6 - 8$ eV, the d^{18} singlet component is maximized, beyond which d^{18} triplet excitations begin to contribute. For physical values of the Coulomb repulsion of Cu $3d$ orbitals ($U \approx 6 - 8$ eV in the case of both molecules²⁷ and solids²⁸), we find that oxyHc is in a dominant d^{18} singlet state ($\approx 50\%$ weight in the singlet multiplet), with d^{19} charge excitations. This is further corroborated by the measurement of the spin correlator $K = 2\langle \mathbf{S}_1 \cdot \mathbf{S}_2 \rangle$ (Fig. 3), which reaches half the saturation value for $U = 6 - 8$ eV. Note that the saturation value would only be obtained for a diatomic system in vacuum, which is not hybridized to the rest of the molecule. As the local Cu $3d$ orbital charge and spin are not true quantum numbers in the molecule, as the two atoms are hybridized, quantum fluctuations reduce the amplitude of the spin correlator to half the full value. This is consistent with the presence of $\approx 50\%$ combined d^{19} and d^{20} excitations (Fig. 2).

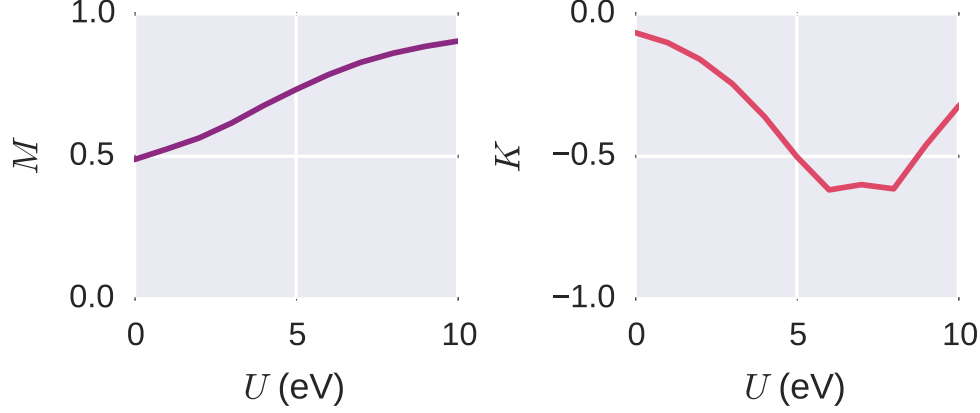


Figure 3: The effective magnetic moment $M = \sqrt{\langle \mathbf{S}_1^2 \rangle / 3}$ (normalized by saturation value) and the spin-correlation $K = 2\langle \mathbf{S}_1 \cdot \mathbf{S}_2 \rangle$ for varying values of the Hubbard U . For a pure two orbital singlet, $K = -1.5$. In our calculations, as the rest of the molecule hybridizes with the Cu orbitals, the spin-correlation is re-normalized to half its saturation value for $U = 6 - 8$ eV.

Von Neumann entropy. The accumulation of possible excitations can be quantified by the Von Neumann entropy. This provides a measure to identify whether the system is actually in a highly mixed quantum state with a multitude of other significant components. The Von Neumann entropy, obtained in the di-Cu $3d$ subspace, reads as: $\Lambda = -\text{Tr} [\hat{\rho}_d \log \hat{\rho}_d]$, where $\hat{\rho}_d$ is the di-Cu reduced finite-temperature density matrix, traced over the states of the AIM bath environment (Fig. 4). Interestingly, we find that the entanglement entropy increases monotonically in the range $U = 0 - 10$ eV. We report the presence of two plateaus, for $U = 4 - 6$ eV and $U = 7 - 8$ eV, that coincide with the formation of the singlet and triplet configurations in the histogram in Fig. 2.

Lifetime of charge excitations. We note that the singlet, in oxyHc, is obtained by super-exchange processes. Direct hopping between localized d-orbitals is very unlikely due to the large

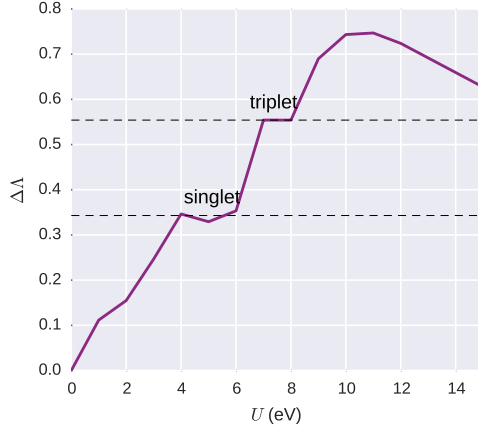


Figure 4: The Von Neumann entropy Λ of the reduced density matrix and its dependence on the on-site interaction U .

distance by which they are separated, and therefore hopping must proceed via an intermediate p-orbital.²⁹ The super-exchange process is usually pictured in the canonical hydrogen atom dimer system. This system describes a pair of up and down electrons that form a singlet state. In this picture, two different limits are possible: i) when the H atoms form a bond at short distance, and the up and down electron form a delocalized bound singlet (BS) centered on the bond, with a high degree of double occupancy, ii) in the dissociated case, known as the Heitler-London (HL) limit, where the H atoms are far apart and the singlet is a true quantum entangled state of the singly occupied H orbitals. In the latter case, the molecular orbital contains only one electron and double occupancy is zero. Although this transition is known in archetypal systems such as the H_2 molecule, few examples in nature are known to exhibit the BS-HL transition. In the HL limit, the charge is typically localized around the H atoms, and typically occurs in the limit of dissociation. However, this effect may also occur in systems where the local Hubbard Coulomb repulsion U

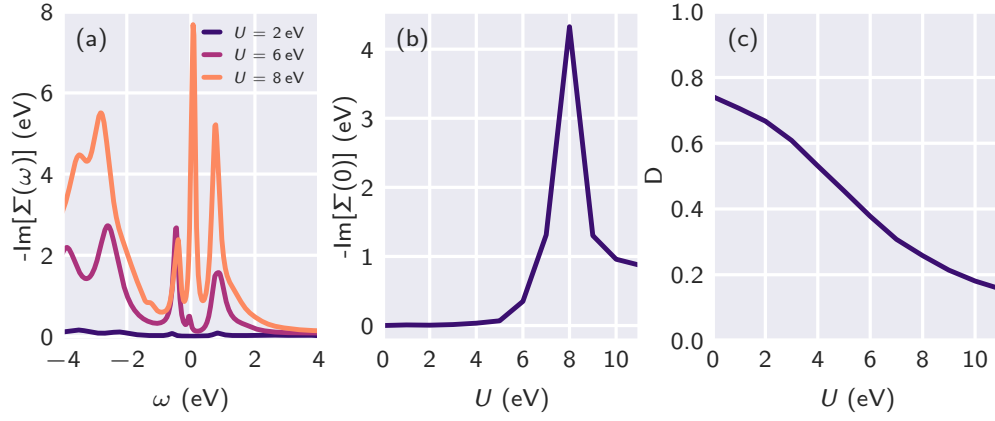


Figure 5: a) Imaginary part of the dynamical mean field local self energy of the Cu-3d empty orbital ($\Sigma''(\omega)$) for Hubbard $U = 2$ eV, 6 eV, and 8 eV. At $U = 8$ eV, we obtain incoherent excitations at $\omega = 0$ eV. b) Self energy at $\omega = 0$ and c) double occupancy D as a function of U . Note that although the double occupancy is evolving smoothly with the Coulomb interaction U , $\Sigma(\omega = 0)$ shows a sharp increase near $U = 8$, that we associate with the stabilization of a localized singlet.

acts as a Coulomb blockage: many-body effects prevent long-lived charge transfer excitations, and the the Coulomb repulsion energy is reduced at the expense of the kinetic energy. A signature of the blockage is typically a large increase in the self energy at the Fermi level (pole structure), indicating charge localization and incoherent scattering associated with a short lifetime of charge excitations.

To investigate the nature of the singlet (BS or HL), we report in Fig. 5(a) the computed self energy of the Cu $3d$ subspace, for various values of U . We obtain a qualitative difference between $U = 6$ eV and $U = 8$ eV, where at $U = 8$ eV the self energy develops a pole at $\omega = 0$. The formation of the pole is particular to $U = 8$ eV (Fig. 5(b)), and is associated with the regime where excitations are incoherent, which prevents long-lived charge transfer excitations from the Cu $3d$ orbitals to O_2 . In this limit, the many body effect acts as a Coulomb blockade and the charge is in turn localized, with weak direct coupling (HL limit). For $U = 6$ eV, the singlet is in the BS limit, where charge excitations allow a direct electron transfer across the oxo-bridge. Note that the observation of the BS-HL crossover is not apparent in averaged quantities, such as in the double occupancies (Fig. 5(c)), which evolve smoothly with the Coulomb repulsion.

Optical transitions. As a further validation of the DFT+DMFT computational model, and to identify the strength of correlations in oxyHc, we extracted the optical absorption spectrum of ligated hemocyanin (Fig. 6). As experiments are performed in the gaseous phase and not in a single crystal, we have calculated the isotropic and anisotropic components of the dielectric tensor. The former involves only pair correlators along the same spatial directions, whereas the latter

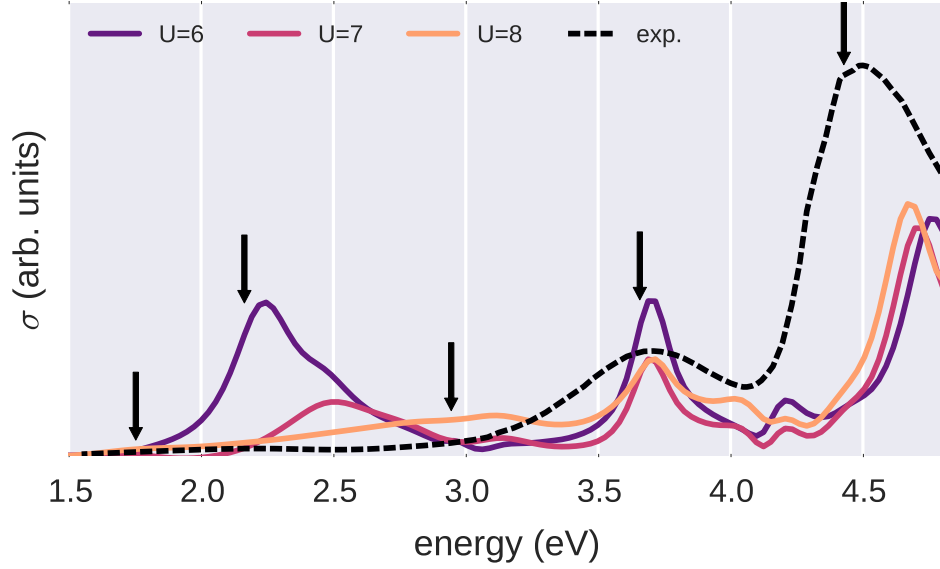


Figure 6: Theoretical optical absorption of the Cu_2O_2 core and imidazole rings obtained by DMFT for values of the Coulomb repulsion $U = 6\text{eV}$, 7eV and 8eV . For comparison, we show the experimental optical absorption obtained by UV-Vis ³⁰ in a wide range of wavelengths (infrared to UV).

also incorporates non-diagonal terms (note that both are causal quantities), which are important in oxyHc as the local coordination axes of the Cu atoms are not aligned. The arrows highlight the positions of the resonances reported by experiments. Remarkable agreement is obtained for $U = 8\text{eV}$, with however a blue shift at high frequency ($\omega > 4\text{eV}$), and a concomitant transfer of optical weight to lower energies ($\omega < 3\text{eV}$). Note however that the positions of the peaks at approximately 3.5eV and 4.5eV are in excellent agreement. The experimental features at 3eV (see arrow) are clearly visible in the theoretical calculations. The peaks at 1.8eV and 2.2eV contribute to the long infrared tail of the optical weight down to 1.5eV . We note that the main difference, between

the BS ($U = 6$ eV) and the HL singlet ($U = 8$ eV), is the presence of a peak associated with charge transfer from ligand to Cu $3d$ orbitals at 2 eV, which is absent in experiment. This strongly associates oxyHc with the HL limit, as numerous optical studies have confirmed the absence of this feature. The suppression of the optical weight at 2eV is due to a large increase in incoherent scattering at $\omega = 0$ eV at $U = 8$ eV (Fig. 5). This is associated with a localization of the holes in the Cu $3d$ shell at $U = 8$ eV. The strong suppression of the optical weight in the near infrared-regime ($\omega < 2$ eV), and the consistent agreement with our calculations, shows that the di-Cu singlet is in the HL regime, and is stabilized via scattering processes.

Characterization of optical transitions. To identify the features present in the optical absorption spectrum, we now turn to the discussion of the spectral weight (Fig. 7). The absorption spectrum of this protein has been reported experimentally to be qualitatively dependent on its ligation state. In its oxygenated form, a weak peak at 570 nm (approximately 2.2 eV, see arrow) corresponds to ligand-to-metal charge transfer^{31,32} from the O_2 π anti-bond with lobes oriented perpendicular to the metal atoms. This orbital is denoted “ π_v^* ”; the π anti-bond with lobes directed towards the copper atoms is denoted π_σ^* and is responsible for an experimentally observed (much stronger) peak at approximately 3.7 eV. Our calculations associate the 2 eV peak in the optical absorption spectrum with a transition from the weight at -1 eV in the density of states (Fig. 7), which is localized on Cu_A/Cu_B /imidazole, to the LUMO. In our calculations, the LUMO is a hybridized state between the Cu and the O_2 , with dominant Cu $3d$ character. We therefore associate the optical weight at 2eV with d-d transitions mediated by charge transfer across the oxo-bridge (although the optical transition from Cu_A to Cu_A is optically dark, that from Cu_A to Cu_B is not). We observe that

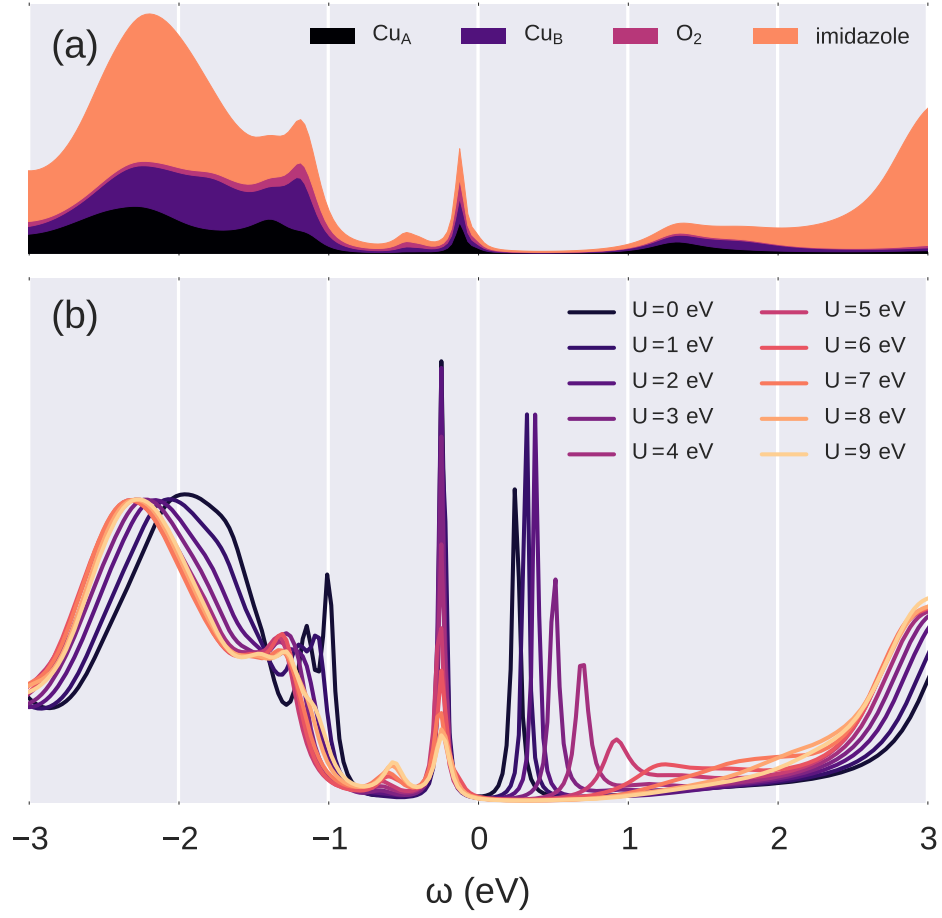


Figure 7: (a) The local density of states for $U = 8$ eV and (b) the different total density of states of the system for a range of Hubbard U values from DMFT.

the increasing U disfavors charge transfer into the Cu $3d$ subspace, and this is manifested in the optical absorption by the reduction of the optical weight at 2eV. The comparison with experiments allows us to identify U precisely with $U = 8$ eV. We note also that DFT, without extensions, puts a strong emphasis on the near infrared peak in the optical absorption. This peak corresponds to Cu-Cu charge transfer across the oxo-bridge. However, as the aforementioned scattering processes are absent at this level of theory, it produces coherent resonances across the HOMO-LUMO gap, observed in the optical spectra at 1.5eV, but absent in experiments.

Molecular bonding. In order to understand the nature of the bonding in the Cu_2O_2 complex, natural bond orbital (NBO) analysis was performed on the DFT and DMFT electronic densities.^{33–35} This involves a series of diagonalization and occupancy-weighted orthogonalization procedures on the single-particle density matrix, transforming it into a set of atom-centered orthogonal natural atomic orbitals (NAOs), then natural hybrid orbitals, and finally the natural bond orbitals $\{|\sigma_i\rangle\}$, which are either one- or two-atom centered. By construction, this procedure decomposes the electronic density into terms resembling Lewis-type chemistry (with bonding and lone pairs of electrons). For hemocyanin, this analysis reveals a hole in one $3d$ orbital for each Cu atom (with $3d$ occupancies of 9.11 and 9.07 for $U = 8$ eV), confirming the expected Cu(II) oxidation state $3d^9 4s^0$ (Figure 8(a)).

A second-order perturbation analysis detects multiple energetically favorable transfers of electronic density from filled to unfilled NBOs, revealing those aspects of the electronic structure that are not well described by Lewis-like chemistry. Early studies of hemocyanin identified

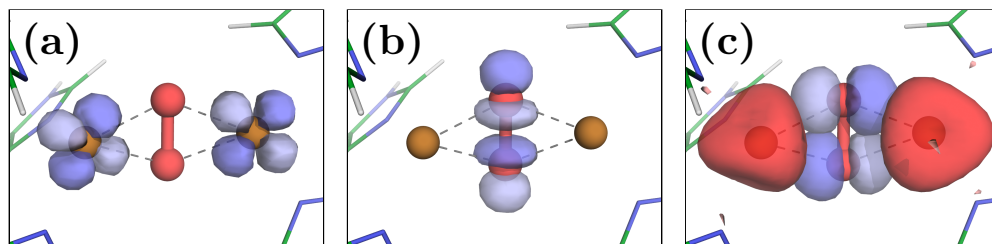


Figure 8: Isosurfaces of several natural bonding orbitals for $U = 8$ eV. (a) Two Cu $3d$ orbitals are identified as half-filled by the NBO analysis. (b) The O_2 σ^* anti-bond is empty, and does not hybridize with any Cu orbitals. (c) Instead, O $2p$ (blue) to Cu $4s$ (red) charge transfer is favorable.

back-bonding charge transfer from Cu $3d$ to oxygen σ^* anti-bonding orbitals (Figure 8(b)) as an important factor in explaining the comparatively low 750 cm^{-1} Raman frequency of the O_2 bond.³⁶ However, our second-order perturbation analyses find that this back-transfer is not present. For $U = 8$ we instead detect favorable charge transfer from O $2p$ orbitals to Cu $4s$ orbitals (Figure 8(c)).

Conclusions

We have presented the application of a DFT + cluster DMFT approach, designed to treat strong electronic interaction and multi-reference effects, to oxyHc, a molecule of important biological function. NBO analysis revealed a hole in one $3d$ orbital for each Cu atom, confirming the expected Cu(II) oxidation state ($3d^9 4s^0$). The reduced density matrix of the $3d$ subspace of the two Cu atoms revealed the presence of fluctuating spin-states, in which a Cu_2 d^{18} singlet component is maximized at $U = 8$ eV. When quantifying the highly mixed quantum state, we observed the formation of

singlet and triplet states in the Von Neumann entropy of the reduced density matrix at different U . Our approach reproduced the experimentally-observed peaks in the absorption spectrum at around 2.2 eV, 3.7 eV and 5.2 eV. NBO analysis revealed that the hybridization of the Cu $4s$ and O $2p$ orbitals is much more favorable than O₂ σ^* orbital back-bonding.

We have found that the Hubbard U is necessary to capture the multi-reference character of the ground-state, placing oxyHc in the limit of a true quantum entangled singlet in the limit of the Heitler-London model. We solve a long-standing problem in the density-functional theory based simulations of type-3 copper systems, which depend heavily on the choice of functional and incorrectly describe multi-reference effects. Our approach, which is implemented in linear-scaling DFT software,³⁷ is optimized to describe transition metal proteins, and hence supports a large range of applications, for example, to enzymes³⁸ or the oxygen-evolving complex (OEC) of photosystem II.³⁹

Methods

The geometry of the 58 atom system was obtained from the literature.¹⁰ This had been optimized using the B3LYP hybrid functional and closely matches the experimentally observed structure.^{10,40}

The DFT ground-state was obtained using ONETEP^{19,41,42}, which is a linear-scaling DFT code that is formally equivalent to a plane-wave method. This is achieved by the *in situ* variational optimization of its atom-centered basis set (spatially-truncated nonorthogonal generalized Wannier functions, or NGWFs).⁴³ The total energy is directly minimized with respect to the NGWFs and the

single-particle density matrix. The use of a minimal, optimized Wannier function representation of the density-matrix allows for the DFT ground state to be solved with relative ease in large systems. This is particularly useful in molecules, since explicit truncation of the basis functions ensures that the addition of vacuum does not increase the computational cost.

The DFT calculations of the oxyHc system were run with an energy cut-off of 897 eV, and with 9 NGWFs on the copper atoms, four on each carbon/nitrogen/oxygen, and one on each hydrogen. Spin symmetry was imposed. All NGWFs employed 7 Å cutoff radii. Open boundary conditions were achieved via a padded cell and a Coulomb cut-off.⁴⁴ The Hubbard projectors were constructed from the Kohn-Sham solutions to an isolated copper pseudopotential.⁴⁵ The pseudopotentials were generated with the OPIUM pseudopotential generation project.⁴⁶

We refined our DFT calculations using the DFT + DMFT method^{16,47} in order to obtain a more accurate treatment of strong electronic correlation effects. In particular, DMFT introduces both quantum and thermal fluctuations, which are multi-reference effects not captured at the level of Kohn-Sham DFT. The oxyHc model was mapped, within DMFT, to an Anderson impurity model (AIM) Hamiltonian,⁴⁸ and we used a recently developed extended Lanczos solver⁴⁹ to obtain the DMFT self energy.

To identify the best spatial representation of the local d -space in the projected Anderson impurity model, we first identified the orthogonal transformation which reduces the off-diagonal elements of the local Green’s function, for respectively the Cu_A and Cu_B sites. Then, we implemented a minimization procedure which finds the closest corresponding real space $SO(3)$ rotation

of the local Cartesian axis corresponding to the $O(5)$ orthonormal transformation in d -space. This provides a unique set of local axes, different on each Cu atoms, which make the local Green's function nearly diagonal in frequency space. As a result, we observed that the Cu_A and Cu_B holes are of pure orbital character within the local axis representation.

Since only a single impurity site ($3d$ orbital subspace) is present, the system becomes crystal momentum independent in the molecular limit, and since the Kohn-Sham Green's function is computed in full, by inversion, before projection onto the impurity subspace, the Anderson impurity mapping is effectively exact, and the necessity of invoking the DMFT self-consistency is not required. However, in DFT+DMFT there is also a charge self-consistency cycle, where (i) the chemical potential can be updated to ensure particle conservation and/or (ii) the DFT+DMFT density kernel can be used to generate a new Kohn-Sham Hamiltonian, which in turn provides a new input to the DMFT; the procedure being repeated until convergence is achieved.^{50–52} In this work, we updated the chemical potential but not the Hamiltonian due to computational cost.

Example input and output files for the DFT and DMFT calculations can be found in the supplementary materials.

To obtain the Kohn-Sham Green's function, we performed the matrix inversion, as well as all matrix multiplications involved in the DMFT algorithm, on graphical processing units (GPUs) using a tailor-made parallel implementation of the Cholesky decomposition written in the CUDA programming language. Electronic correlation effects are described within the localized subspace

by the Slater-Kanamori form of the Anderson impurity Hamiltonian,^{53,54} specifically:

$$\begin{aligned} \mathcal{H}_U = & U \sum_m n_{m\uparrow} n_{m\downarrow} + \left(U' - \frac{J}{2} \right) \sum_{m>m'} n_m n_{m'} \\ & - J \sum_{m>m'} \left(2\mathbf{S}_m \mathbf{S}_{m'} + \left(d_{m\uparrow}^\dagger d_{m\downarrow}^\dagger d_{m'\uparrow} d_{m'\downarrow} \right) \right), \end{aligned} \quad (1)$$

where m, m' are orbital indices, $d_{m\sigma}$ ($d_{m\sigma}^\dagger$) annihilates (creates) an electron with spin σ in the orbital m , and n_m is the orbital occupation operator.

The first term describes the effect of intra-orbital Coulomb repulsion, parametrized by U , and the second term describes the inter-orbital repulsion, proportional to U' , which is renormalized by the Hund's exchange coupling parameter J in order to ensure a fully rotationally invariant Hamiltonian (for further information on this topic, we refer the reader to Ref. 55). The third term is the Hund's rule exchange coupling, described by a spin exchange coupling of amplitude J . \mathbf{S}_m denotes the spin corresponding to orbital m , so that $\mathbf{S}_m = \frac{1}{2} d_{ms}^\dagger \vec{\sigma}_{ss'} d_{ms'}$, where $\vec{\sigma}$ is the vector of Pauli matrices.

Our DMFT calculations were carried out at room temperature, $T = 293$ K and the Hubbard U was varied in the range 0 - 10 eV, with a fixed Hund's coupling $J = 0.8$ eV. The theoretical optical absorption was obtained in DFT + DMFT within the linear-response regime (Kubo formalism), in the *no-vertex-corrections* approximation,⁵⁶ which is given by:

$$\begin{aligned} \sigma(\omega) = & \frac{2\pi e^2 \hbar}{\Omega} \int d\omega' \frac{f(\omega' - \omega) - f(\omega')}{\omega} \\ & \times \left(\rho^{\alpha\beta}(\omega' - \omega) \mathbf{v}_{\beta\gamma} \rho^{\gamma\delta}(\omega') \cdot \mathbf{v}_{\delta\alpha} \right), \end{aligned} \quad (2)$$

and the factor of two accounts for spin-degeneracy, Ω is the simulation-cell volume, e is the elec-

tron charge, \hbar is the reduced Planck constant, $f(\omega)$ is the Fermi-Dirac distribution, and $\rho^{\alpha\beta}$ is the density-matrix given by the frequency-integral of the interacting DFT + DMFT Green's function. The matrix elements of the velocity operator, $\mathbf{v}_{\alpha\beta}$, noting that we do not invoke the Peierls substitution,⁵⁶ are given by:

$$\mathbf{v}_{\alpha\beta} = -\frac{i\hbar}{m_e} \langle \phi_\alpha | \nabla | \phi_\beta \rangle + \frac{i}{\hbar} \langle \phi_\alpha | [\hat{V}_{nl}, \mathbf{r}] | \phi_\beta \rangle. \quad (3)$$

This expression is general to the NGWF representation,⁵⁷ used in this work, where the contribution to the non-interacting Hamiltonian due to the non-local part of the norm-conserving pseudopotentials,^{58,59} represented by \hat{V}_{nl} , is included.

Finally, the double-counting correction E_{DC} must be introduced, since the contribution of interactions between the correlated orbitals to the total energy is already partially included in the exchange-correlation potential derived from DFT. The most commonly used form of the double-counting term is⁶⁰:

$$E_{dc} = \frac{U^{av}}{2} n_d (n_d - 1) - \frac{J}{2} \sum_{\sigma} n_{d\sigma} (n_{d\sigma} - 1). \quad (4)$$

The natural bonding orbital analysis was performed using the *NBO 5* programme³⁴. Performing this transformation starting from ONETEP's basis of NGWFs is non-trivial, and is described in Ref. 35. The NBOs generated from DFT + DMFT densities largely retain the familiar profile of DFT-based NBOs, but their occupancies may be expected to deviate further from integer values due to quantum-mechanical and finite-temperature multi-reference effects captured within DFT + DMFT.

1. Solomon, E. I. *et al.* Copper Active Sites in Biology. *Chemical Reviews* **114**, 3659–3853 (2014).
2. Yoon, J., Fujii, S. & Solomon, E. I. Geometric and electronic structure differences between the type 3 copper sites of the multicopper oxidases and hemocyanin/tyrosinase. *Proceedings of the National Academy of Sciences* **106**, 6585–6590 (2009). <http://www.pnas.org/content/106/16/6585.full.pdf>.
3. McGivern, T., Afsharpour, S. & Marmion, C. Copper complexes as artificial dna metallonucleases: From sigmans reagent to next generation anti-cancer agent? *Inorganica Chimica Acta* **472**, 12 – 39 (2018).
4. Nunes, C. J. *et al.* Reactivity of dinuclear copper(ii) complexes towards melanoma cells: Correlation with its stability, tyrosinase mimicking and nuclease activity. *Journal of Inorganic Biochemistry* **149**, 49 – 58 (2015).
5. Gherman, B. F. & Cramer, C. J. Quantum chemical studies of molecules incorporating a $\text{Cu}_2\text{O}_2^{2+}$ core. *Coordination Chemistry Reviews* **253**, 723–753 (2009).
6. Dooley, D. M., Scott, R. A., Ellinghaust, J., Solomont, E. I. & Gray, H. B. Chemistry Magnetic susceptibility studies of laccase and oxyhemocyanin (copper proteins/variable temperature measurements/antiferromagnetism). *Proceedings of the National Academy of Sciences of the United States of America* **75**, 3019–3022 (1978).
7. Solomon, E. I. *et al.* Copper dioxygen (bio)inorganic chemistry. *Faraday discussions* **148**, 11–39; discussion 97–108 (2011).

8. Takano, Y. *et al.* Theoretical studies on the magnetic interaction and reversible dioxygen binding of the active site in hemocyanin. *Chemical physics letters* **335**, 395–403 (2001).
9. Metz, M. & Solomon, E. I. Dioxygen binding to deoxyhemocyanin: electronic structure and mechanism of the spin-forbidden two-electron reduction of O_2 . *Journal of the American Chemical Society* **123**, 4938–4950 (2001).
10. Saito, T. & Thiel, W. Quantum Mechanics/Molecular Mechanics study of oxygen binding in hemocyanin. *The Journal of Physical Chemistry B* **118**, 5034–5043 (2014).
11. Cohen, A. J., Tozer, D. J. & Handy, N. C. Evaluation of in density functional theory Evaluation of $\langle \hat{S}^2 \rangle$ in density functional theory. *The Journal of Chemical Physics* **126**, 214104–130901 (2007).
12. Cramer, C. J., Kinal, A., Włoch, M., Piecuch, P. & Gagliardi, L. Theoretical characterization of end-on and side-on peroxide coordination in ligated Cu_2O_2 models. *The Journal of Physical Chemistry A* (2006).
13. Cramer, C. J., Włoch, M., Piecuch, P., Puzzarini, C. & Gagliardi, L. Theoretical models on the Cu_2O_2 torture track: Mechanistic implications for oxytyrosinase and small-molecule analogues. *The Journal of Physical Chemistry A* (2006).
14. Siegbahn, P. E. M. The performance of hybrid DFT for mechanisms involving transition metal complexes in enzymes. *JBIC Journal of Biological Inorganic Chemistry* **11**, 695–701 (2006).
15. Loeb L, B., Crivelli P, I. & Andrade P, C. Oxy-hemocyanin: A peroxo copper (ii) complex? a mixed-valence alternative view. *Comments on Inorganic Chemistry* **20**, 1–26 (1998).

16. Georges, A., Kotliar, G., Krauth, W. & Rozenberg, M. J. Dynamical mean-field theory of strongly correlated fermion systems and the limit of infinite dimensions. *Reviews of Modern Physics* **68**, 13 (1996).
17. Lin, N., Marianetti, C. A., Millis, A. J. & Reichman, D. R. Dynamical mean-field theory for quantum chemistry. *Physical Review Letters* **106**, 096402 (2011).
18. Jacob, D., Haule, K. & Kotliar, G. Dynamical mean-field theory for molecular electronics: Electronic structure and transport properties. *Physical Review B* **82**, 5 (2010).
19. Hine, N. D. M., Haynes, P. D., Mostofi, A. A., k. Skylaris, C. & Payne, M. C. Linear-scaling density-functional theory with tens of thousands of atoms: Expanding the scope and scale of calculations with onetep. *Computer Physics Communications* **180**, 1041–1053 (2009).
20. Weber, C. *et al.* Vanadium dioxide : A peierls-mott insulator stable against disorder. *Physical Review Letters* **108**, 2 (2012).
21. Linscott, E. B., Cole, D. J., Hine, N. D. M., Payne, M. C. & Weber, C. Introducing TOSCAM: uniting dynamical mean field theory and linear-scaling density functional theory. *in preparation* (2018).
22. Weber, C. *et al.* Importance of many-body effects in the kernel of hemoglobin for ligand binding. *Physical Review Letters* **110**, 106402 (2013).
23. Weber, C., Cole, D. J., O'Regan, D. D. & Payne, M. C. Renormalization of myoglobin–ligand binding energetics by quantum many-body effects. *Proceedings of the National Academy of Sciences* 201322966 (2014).

24. Scherlis, D. A., Cococcioni, M., Sit, P. & Marzari, N. Simulation of heme using DFT + U: A step toward accurate spin-state energetics. *The Journal of Physical Chemistry B* **111**, 7384–7391 (2007).
25. Zaanen, J. *et al.* What can be learned about high- T_c from local density theory. *Physica C* **153**, 1636 (1988).
26. Annett, J. F., Martin, R. M., McMahan, A. & Satpathy, S. Electronic hamiltonian and antiferromagnetic interactions in La_2CuO_4 . *Physical Review B* **40**, 2620 (1989).
27. Didziulis, S. V., Cohen, S. L., Gewirth, A. A. & Solomon, E. I. Variable photon energy photoelectron spectroscopic studies of copper chlorides: an experimental probe of metal-ligand bonding and changes in electronic structure on ionization. *Journal of the American Chemical Society* **110**, 250–268 (1988).
28. Anisimov, V. I., Zaanen, J. & Andersen, O. K. Band theory and mott insulators: Hubbard U instead of stoner i . *Physical Review B* **44**, 943–954 (1991).
29. Pavarini, E., Koch, E., Anders, F. & Jarrel, M. From models to materials. modeling and simulation. *Chemical physics letters* **Vol. 2** (2012).
30. Andersen, N. H., Zoppellaro, G., Bubacco, L., Casella, L. & Andersson, K. K. Raman, uv–vis, and cd spectroscopic studies of dodecameric oxyhemocyanin from *carcinus aestuarii*. *Chemistry letters* **40**, 1360–1362 (2011).

31. Himmelwright, R. S., Eickman, N. C., LuBien, C. D. & Solomon, E. I. Chemical and spectroscopic comparison of the binuclear copper active site of mollusc and arthropod hemocyanins. *Journal of the American Chemical Society* **102**, 5378–5388 (1980).
32. Heirwegh, K., Borginon, H. & Lontie, R. Separation and absorption spectra of α - and β -haemocyanin of *Helix pomatia*. *Biochimica et biophysica acta* **48**, 517–526 (1961).
33. Reed, A. E., Curtiss, L. A. & Weinhold, F. Intermolecular interactions from a natural bond orbital, donor-acceptor viewpoint. *Chemical Reviews* **88**, 899–926 (1988).
34. Glendening, E. D. *et al.* NBO 5.9 and the NBO 5.9 Manual (2011). URL <http://www.chem.wisc.edu/~nbo5>.
35. Lee, L. P., Cole, D. J., Payne, M. C. & Skylaris, C. Natural bond orbital analysis in the onetep code: Applications to large protein systems. *Journal of Computational Chemistry* **34**, 429–444 (2013).
36. Baldwin, M. J. *et al.* Spectroscopic studies of side-on peroxide-bridged binuclear copper(II) model complexes of relevance to oxyhemocyanin and oxytyrosinase. *Journal of the American Chemical Society* **114**, 10421–10431 (1992).
37. Cole, D. J. & Hine, N. D. Applications of large-scale density functional theory in biology. *Journal of Physics: Condensed Matter* **28**, 393001 (2016).
38. Ermler, U., Grabarse, W., Shima, S., Goubeaud, M. & Thauer, R. K. Active sites of transition-metal enzymes with a focus on nickel. *Current Opinion in Structural Biology* **8**, 749–758 (1998).

39. Suga, M. *et al.* Native structure of photosystem II at 1.95 Å resolution viewed by femtosecond X-ray pulses. *Nature* **517**, 99–103 (2015).
40. Magnus, K. A. *et al.* Crystallographic analysis of oxygenated and deoxygenated states of arthropod hemocyanin shows unusual differences. *Proteins: Structure, Function, and Bioinformatics* **19**, 302–309 (1994).
41. O'Regan, D. D., Hine, N. D. M., Payne, M. C. & Mostofi, A. A. Linear-scaling dft+*u* with full local orbital optimization. *Physical Review B* **85**, 085107 (2012).
42. Hine, N. D. M., Haynes, P. D., Mostofi, A. A. & Payne, M. C. Linear-scaling density-functional simulations of charged point defects in Al_2O_3 using hierarchical sparse matrix algebra. *Journal of Chemical Physics* **133**, 11 (2010).
43. Skylaris, C., Mostofi, A. A., Haynes, P. D., Diéguez, O. & Payne, M. C. Nonorthogonal generalized wannier function pseudopotential plane-wave method. *Physical Review B* **66**, 035119 (2002).
44. Hine, N. D. M., Dziedzic, J., Haynes, P. D. & Skylaris, C.-K. Electrostatic interactions in finite systems treated with periodic boundary conditions: Application to linear-scaling density functional theory. *Journal of Chemical Physics* **135** (2011).
45. Ruiz-Serrano, Á., Hine, N. D. M. & Skylaris, C.-K. Pulay forces from localized orbitals optimized in situ using a psinc basis set. *Journal of Chemical Physics* **136**, 234101 (2012).
46. Rappe, A. M., Rabe, K. M., Kaxiras, E. & Joannopoulos, J. D. Optimized pseudopotentials. *Phys. Rev. B* **41**, 1227–1230 (1990).

47. Maier, T. A., Pruschke, T. & Jarrell, M. Angle-resolved photoemission spectra of the hubbard model. *Physical Review B* **66**, 7 (2002).
48. da Silva, L. G. G. V. D., Tiago, M. L., Ulloa, S. E., Reboredo, F. A. & Dagotto, E. Many-body electronic structure and kondo properties of cobalt-porphyrin molecules. *Physical Review B* **80**, 3 (2009).
49. Aichhorn, M., Daghofer, M., Evertz, H. G. & von der Linden, W. Low-temperature lanczos method for strongly correlated systems. *Physical Review B* **67**, 3 (2003).
50. Pourovskii, L. V., Amadon, B., Biermann, S. & Georges, A. Self-consistency over the charge density in dynamical mean-field theory: A linear muffin-tin implementation and some physical implications. *Physical Review B* **76**, 1 (2007).
51. Park, H., Millis, A. J. & Marianetti, C. A. Computing total energies in complex materials using charge self-consistent DFT + DMFT. *Physical Review B* **90**, 235103 (2014).
52. Bhandary, S., Assmann, E., Aichhorn, M. & Held, K. Charge self-consistency in density functional theory combined with dynamical mean field theory: k -space reoccupation and orbital order. *Physical Review B* **94**, 155131 (2016).
53. Slater, J. C. The ferromagnetism of nickel. *Physical Review* **49**, 537–545 (1936).
54. Kanamori, J. Superexchange interaction and symmetry properties of electron orbitals. *Journal of Physics and Chemistry of Solids* **10**, 87–98 (1959).

55. Imada, M., Fujimori, A. & Tokura, Y. Metal-insulator transitions. *Reviews of Modern Physics* **70**, 1039 (1998).
56. Millis, A. J. Optical conductivity and correlated electron physics. *Strong Interactions in Low Dimensions, Physics and Chemistry of Materials with Low-Dimensional Structures* **25**, 195 (2004).
57. Halpern, V. & Bergmann, A. Calculation of electronic green functions using nonorthogonal basis functions: application to crystals. *Journal of Physics C: Solid State Physics* **5**, 15 (1972).
58. Ratcliff, L. E., Hine, N. D. M. & Haynes, P. D. Calculating optical absorption spectra for large systems using linear-scaling density functional theory. *Physical Review B* **84**, 1 (2011).
59. Read, A. J. & Needs, R. J. Calculation of optical matrix elements with nonlocal pseudopotentials. *Physical Review B* **44**, 13071–13073 (1991).
60. Pruschke, T. & Zöhl, M. Electronic structure and ordered phases in transition metal oxides: application of the dynamical mean-field theory. In *Advances in Solid State Physics* **40**, 251–265 (2000).

Acknowledgements This work was supported by BBSRC (grant BB/M009513/1), EPSRC (grants EP/N02396X/1, EP/L015552/1) and the Rutherford Foundation Trust. The Flatiron Institute is a division of the Simons Foundation. C.W. gratefully acknowledges the support of NVIDIA Corporation with the donation of the Tesla K40 GPUs used for this research. For computational resources, we were supported by the ARCHER UK National Supercomputing Service and the UK Materials and Molecular Modelling Hub for computational resources (EPSRC Grant No. EP/ P020194/1).

Author contributions C. W. and M. A. B. conceived and planned the research. M. A. B., E. B. L and C. W. performed the calculations. All the authors analyzed the data and contributed to the final manuscript.

Competing Interests The authors declare that they have no competing financial interests.

Correspondence Correspondence and requests for materials should be addressed to Mohamed Ali al-Badri (email:mohamed.al-badri@kcl.ac.uk) and Cedric Weber (email:cedric.weber@kcl.ac.uk).

Table 1: DMFT $3d$ orbital occupations of Cu in our model of ligated hemocyanin for different Hubbard U values.

Atom	$d_{x^2-y^2}$	$d_{3z^2-r^2}$	d_{xy}	d_{xz}	d_{yz}
Cu1 ($U = 0$ eV)	2.00	2.00	1.95	1.72	1.93
Cu2 ($U = 0$ eV)	1.68	2.00	1.98	1.99	2.00
Cu1 ($U = 8$ eV)	2.00	2.00	1.95	1.25	1.93
Cu2 ($U = 8$ eV)	1.21	2.00	1.98	1.99	2.00
Cu1 ($U = 10$ eV)	2.00	2.00	1.95	1.18	1.93
Cu2 ($U = 10$ eV)	1.14	2.00	1.98	1.99	2.00